JOURNAL OF COMPUTATIONAL PHYSICS 9, 138–158 (1972)

Numerical Solutions to the Helicon Boundary Value Problem*

N. L. WENTLAND† AND J. R. MERRILL

Department of Physics and Astronomy,
Dartmouth College, Hanover, New Hampshire 03755

Received February 2, 1971

Numerical methods are applied to the helicon boundary value problem. A method of solution is described which is completely general and independent of both the geometry and the detailed form of the resistivity tensor. This approach is applied to two particular geometries under the assumption of a free electron gas model. The first geometry is the infinite plate perpendicular to the magnetic field. In this case excellent agreement with the analytic solution of Chambers and Jones is found. For the second geometry, a finite rectangular parallelepiped, a solution is found which is qualitatively and semi-quantitatively correct. These calculations allow the continued use of helicon experiments to measure topological features of Fermi surfaces in metals. In the absence of calculations such as those presented, crude approximations to the boundary value solution have been used without any way to check their theoretical validity.

1. INTRODUCTION

Under certain conditions electromagnetic radiation can penetrate large distances into highly conductive media. The media must be permeated by a large, static magnetic field, B_0. Alven waves and radio whistlers are examples of this effect in ionospheric plasmas. If the plasma is the electron gas of a metal and condition (1) is met, the waves are called helicons.

$$\omega \ll \nu < \omega_c \ll \omega_p . \tag{1}$$

ω is the wave frequency; ν is the collision frequency; ω_c is the cyclotron frequency; ω_p is the plasma frequency.

In general a conducting medium can be characterized by a resistivity tensor $\boldsymbol{\rho}$. The constitution relation relating the electric field $\mathbf{E}$ and the current density $\mathbf{J}$ can be written as

$$\mathbf{E} = \boldsymbol{\rho}\mathbf{J}. \tag{2}$$

* Work supported by the United States Atomic Energy Commission [Contract No. AT(30-1)-4186].

† Portions of this work formed partial fulfillment of the requirement of the Masters degree for N. L. Wentland.

Combining Eq. (2) with Maxwell's equations we find the helicon wave equation

$$\nabla \times (\rho \nabla \times \mathbf{B}) = -\mu_0(\partial \mathbf{B}/\partial t). \tag{3}$$

In arriving at Eq. (3) we have neglected the displacement current term in Maxwell's equations. This is valid because helicon frequencies are typically of the order of hundreds to thousands of Hertz; displacement currents are important in metals only for frequencies in the infrared (10^{11}Hz and above).

It has been shown [1] that the proper boundary condition at the sample–vacuum interface (in the case of a nonferromagnetic metal) is that all three components of the field be continuous.

$$\mathbf{B} \text{ vacuum/boundary} = \mathbf{B} \text{ helicon/boundary}. \tag{4}$$

In vacuum the fields obey the magnetostatic condition

$$\nabla^2 \mathbf{B} = 0. \tag{5}$$

Equation (5) states that the vacuum fields can respond to changes in the boundary values brought about by the helicon equation, (3), in times short with respect to helicon wave periods. The group velocity in vacuum (that of light, c) is much larger than the group velocity of helicon waves (typically 30 cm/sec).

Equations (3)–(5) together formulate a well-posed boundary value problem. This boundary value problem has been solved in closed form for only two geometries: the infinite cylinder parallel to the static field [2], and the infinite plate perpendicular to B_0 [3].

We now apply numerical methods, specifically the methods of finite differences, to the solution of this boundary value problem. The power of this approach is that it can handle an arbitrary geometry and resistivity tensor.

The remainder of this paper will first discuss applied numerical methods. Secondly, it will use these methods to reproduce the results of Chambers and Jones [3] for the infinite plate geometry. Lastly, we attempt to handle a finite rectangular parallelepiped. In making the application to these two geometries, a free electron gas model is assumed.

2. Numerical Methods

Finite Difference Representation

In its simplest form the method of finite differences consists of replacing each differential element in a partial differential equation with an appropriate set of sums and differences of field quantities. These sets of field quantities are then

assembled according to the partial differential equation into a finite difference equation. This equation (or set of equations) is then solved for unknown quantities and applied iteratively to each lattice point. The lattice is the finite set of points in four space that results from making the continous variables x, y, z, and t discrete. Lattice points are numbered sequentially along the x, y, and z axes and referenced by three integral subscripts I, J and K, respectively. The time level is referenced by the integer N.

From the theory of numerical methods, a finite difference equation must meet three criteria. These are: (1) The finite difference equation must be stable; (2) the finite difference equation must converge to the partial differential equation, in the limit of infinitesimal step sizes; and (3) the finite difference equation must be consistent with (correctly represent) the partial differential equation. Ideally, those criteria could be used to select a finite difference representation. In general this is not possible. In the case of the helicon equation, the stability condition, for example, involves a matrix which is very difficult to interpret. To circumvent these problems, a representation is arbitrarily selected and implemented. If the solution does not numerically diverge, then the other criteria are assumed to be met. This point of view is strengthened by a theorem of numeric theory [4]. This method of trial and error is used in the course of the work.

Several finite difference representations were used. The simplest explicit representation

$$\begin{aligned}(dB/dt) &= [B(K, N+1) - B(K, N)]/\Delta T,\\ (d^2B/dZ^2) &= [B(K+1, N) - 2B(K, N) + B(K-1, N)]/(\Delta Z)^2\end{aligned} \tag{6}$$

was found to be unstable for all values of Δt.
The explicit scheme which uses

$$(dB/dt) = [B(K, N+1) - B(K, N-1)]/2\Delta T \tag{7}$$

was also unstable. The simplest implicit scheme was stable and yielded correct results. The disadvantage of this implicit method was the amount of time and storage required to handle the matrices which must be used.

The method due to Dufort and Frankel [5] proved most successful and is applied to both the infinite plate and the finite plate geometries. The method of Dufort and Frankel makes the following identifications:

$$\begin{aligned}(dB/dt) &= [B(K, N+1) - B(K, N)]/\Delta T,\\ (d^2B/dZ^2) &= [B(K+1, N) - B(K, N-1) - B(K, N+1) + B(K-1, N)]/(\Delta Z)^2\end{aligned} \tag{8}$$

The Computer and Peripheral Equipment

All calculations were performed on the General Electric 635 Computer at Dartmouth. Except where noted, the Time-Sharing system was used. Time-

sharing is a highly interactive system with turnaround times of a few seconds. Input and output is normally received from and directed to a standard teletype machine connected to the computer by a telephone line. The General Electric Mark II FORTRAN programming language was used. Because Mark II FORTRAN and FORTRAN IV are very similar, the user can debug programs under the highly interactive Time-Sharing system. The program can then be turned over for FORTRAN IV batch processing if necessary, with little difficulty.

Plots were generated on a Time-Sharing Devices model C/P 701 plotter/driver. This device consists of a digital to analog converter and an $x - y$ recorder. The plotter was driven by information produced from the computer by subroutines available in the computer's public library.

Program Strategy (*The algorithm*). The solution to the helicon boundary values problem consists of several steps. They are:

Step 1. Specify the initial field distribution, $B(x, y, z)$, at time equal to zero. Turn off all drive fields at this time retaining only the static field B_0, and the internal, constant, helicon field $B(x, y, z)$.

Step 2. Set the fields to zero outside the sample in order to clear the slate for an iterative application of Step 3.

Step 3. Evaluate the fields outside the sample using the magnetostatic condition and the internal fields at the sample surface. (This is a relaxation method.)

Step 4. Re-evaluate the fields in the sample. This re-evaluation will require one application of the helicon equation at each lattice point. The re-evaluation will require some information about fields just outside the sample.

Step 5. Evaluate and print the permeability, μ. Average the internal fields over space.

Step 6. If an end condition is met, execute Step 7; otherwise return to Step 2,

Step 7. Store the field distribution for future use.

3. Application to the Infinite Plate

The first geometry considered is that of an infinite plate. An infinite plate is a sheet with thickness, c, and with infinite length and width. This plate is oriented so that the magnetic field, B_0, and the normal to the plate are along the z axis. The drive field, b, is in the x direction. The helicon will be detected along the x direction after the drive field, b, is turned off. (This is the step-field method for determining

the response. The continuous wave response is the Fourier transform of this step-field response [3]. The origin of coordinates is chosen at the geometric center of the sample (see Fig. 1).

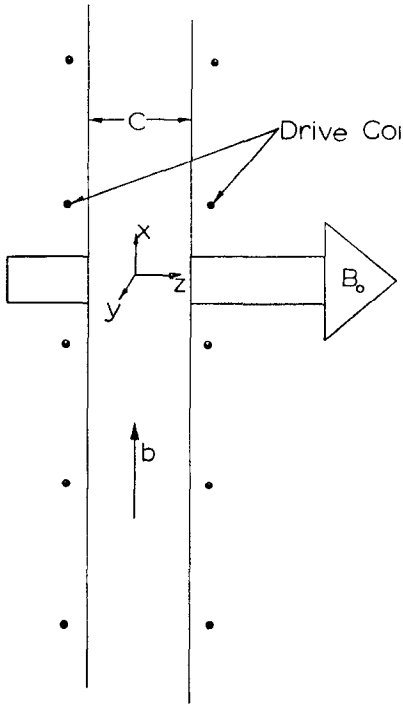

FIG. 1. Experimental arrangement of a step-field helicon experiment with an infinite plot geometry.

For this infinite plate geometry, field quantities vary only with respect to z. All partial derivatives with respect to x and y vanish. The helicon equation (3) then simplifies to two coupled equations in the two unknowns B_x and B_y. They are

$$\begin{aligned} -\rho_{22}(\partial^2 B/\partial z^2)\, x + \rho_{21}(\partial^2 B/\partial z^2)\, y &= -\mu_0(\partial B/\partial t)\, x, \\ -\rho_{11}(\partial^2 B/\partial z^2)\, y + \rho_{12}(\partial^2 B/\partial z^2)\, x &= -\mu_0(\partial B/\partial t)\, y. \end{aligned} \tag{9}$$

As mentioned above, we assume a free electron (jellium) model. A free electron gas is described by a resistivity tensor of the form

$$\rho = \begin{pmatrix} \rho & -RB_0 & 0 \\ RB_0 & \rho & 0 \\ 0 & 0 & \rho \end{pmatrix}. \tag{10}$$

The parameter R is the Hall coefficient for the electron gas. It is traditional (after Chamber and Jones [3]) to define a parameter, u, as

$$u = RB_0/\rho. \tag{11}$$

u is the tangent of the Hall angle. The current density, J, flows at an angle $\tan^{-1}u$ to E. In the limit $u \gg 1$, this angle approaches $\pi/2$ so no energy is lost by Joule heating and helicon waves propagate freely.

The analytic solution to Eq. (9) with Eq. (10) is [3]

$$\frac{B(Z, t)}{B(Z, 0)} = \frac{4}{\pi} \sum_{n\,\text{odd}} \frac{1}{n} i^{n-1} \cos\left(\frac{n\pi z}{c}\right) e^{(i\omega_n t - t/\tau_n)} \tag{12}$$

with $\omega_n = n^2\pi^2 RB_0/c^2\mu_0$ and $1/\tau_n = n^2\pi^2\rho/c^2\mu_0$. The field $B(Z, t)$ has its x and y components combined in this approach as a rotating complex field. B_x is the real part of $B(Z, t)$.

If we make a change of variables

$$\begin{aligned} Z &= z\pi/c \\ T &= \rho_{22}\pi^2 t/\mu_0 c^2 \end{aligned} \tag{13}$$

Eq. (12) becomes

$$\frac{B(Z, T)}{B(Z, 0)} = \frac{4}{\pi} \sum_{n\,\text{odd}} \frac{1}{n} i^{n-1} \cos(nZ)\, e^{-in^2uT} e^{-n^2T}. \tag{14}$$

Integrating (14) over the sample thickness yields

$$\mu \equiv \int \frac{B(Z, T)}{B(Z, 0)}\, dZ = \frac{8}{\pi^2} \sum_{n\,\text{odd}} \frac{1}{n^2} e^{-in^2uT} e^{-n^2T}. \tag{15}$$

The quantity μ, the experimentally detected quantity, is the (complex) permeability for the medium.

Implementation of the Program

Substituting the expressions of Dufort and Frankel [8] into the helicon equation (3) and solving for unknown quantities we obtain

$$\begin{aligned} &B(N + 1, 1, K) \\ &\quad = [\text{TERM 3} + \text{TERM 2} + \text{TERM 1}]/[1 + \text{TERM 3} * \text{TERM 3}] \\ &B(N + L, 2, K) \\ &\quad = -[\text{TERM 3} + \text{TERM 2} - \text{TERM 1}]/[1 + \text{TERM 3} * \text{TERM 3}] \end{aligned} \tag{16a}$$

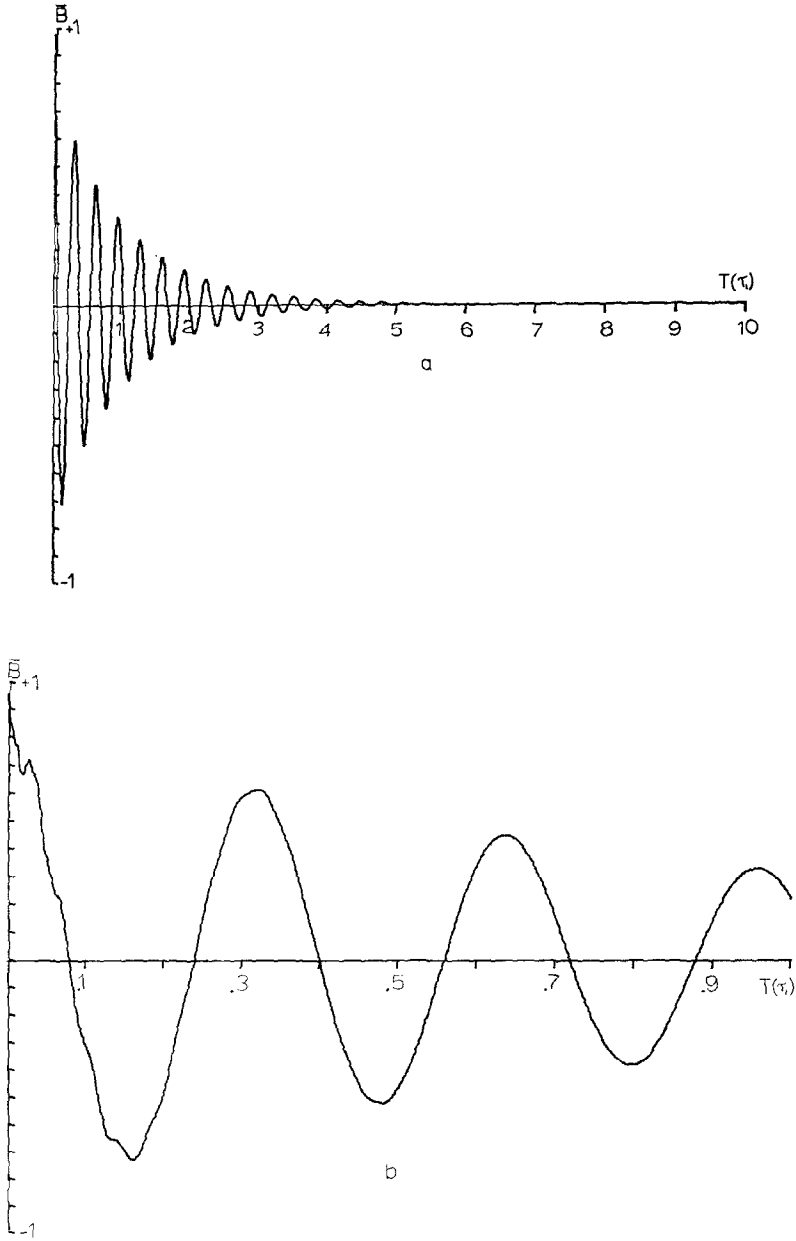

FIG. 2. The step-field response of an infinite plate (under the assumption of a free electron gas) using the methods of finite differences.

where

$$\text{TERM 3} = 2u\lambda/(1 + 2\lambda)$$

$$\begin{aligned}\text{TERM 1} = {} & B(N-1, 1, K)[(1-2\lambda)/(1+2\lambda)] \\ & + 2\lambda[B(N, 1, K+1) + B(N, 1, K-1)]/(1+2\lambda) \\ & - \text{TERM 3}\,[B(N, 2, K+1) - B(N-1, 2, K) + B(N, 2, K-1)]\end{aligned} \tag{16b}$$

$$\begin{aligned}\text{TERM 2} = {} & B(N-1, 2, K)[(1-2\lambda)/(1+2\lambda)] \\ & + 2\lambda[B(N, 2, K+1) + B(N, 2, K-1)]/(1+2\lambda) \\ & \text{TERM 3}\,[B(N, 1, K+1) - B(N-1, 1, K) + B(N, 1, K-1)]\end{aligned}$$

and

$$\lambda = (\Delta T/\Delta Z^2). \tag{16c}$$

In FORTRAN notation the subscripts N, $N+1$, $N-1$ refer to time levels, and the subscripts K, $K+1$, $K-1$ refer to the position along the z axis ($K = 1$ corresponds to the $-(c/2)$ boundary and $K = K\text{MAX}$ corresponds to the $+(c/2)$ boundary). The other subscript (1 or 2) refers to the field component (x component or y component, respectively). This scheme is implemented by program PROG6 and is available from the authors on request [6].

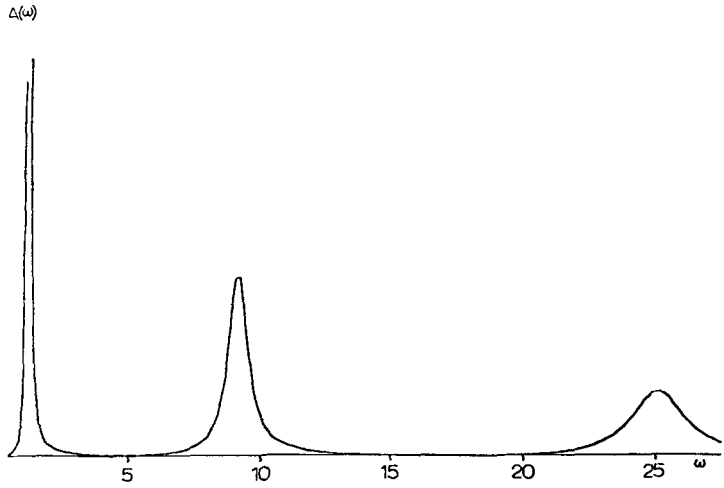

FIG. 3. The continuous wave response of an infinite plate (under the assumption of a free electron gas). The Fourier transform of Fig. 2.

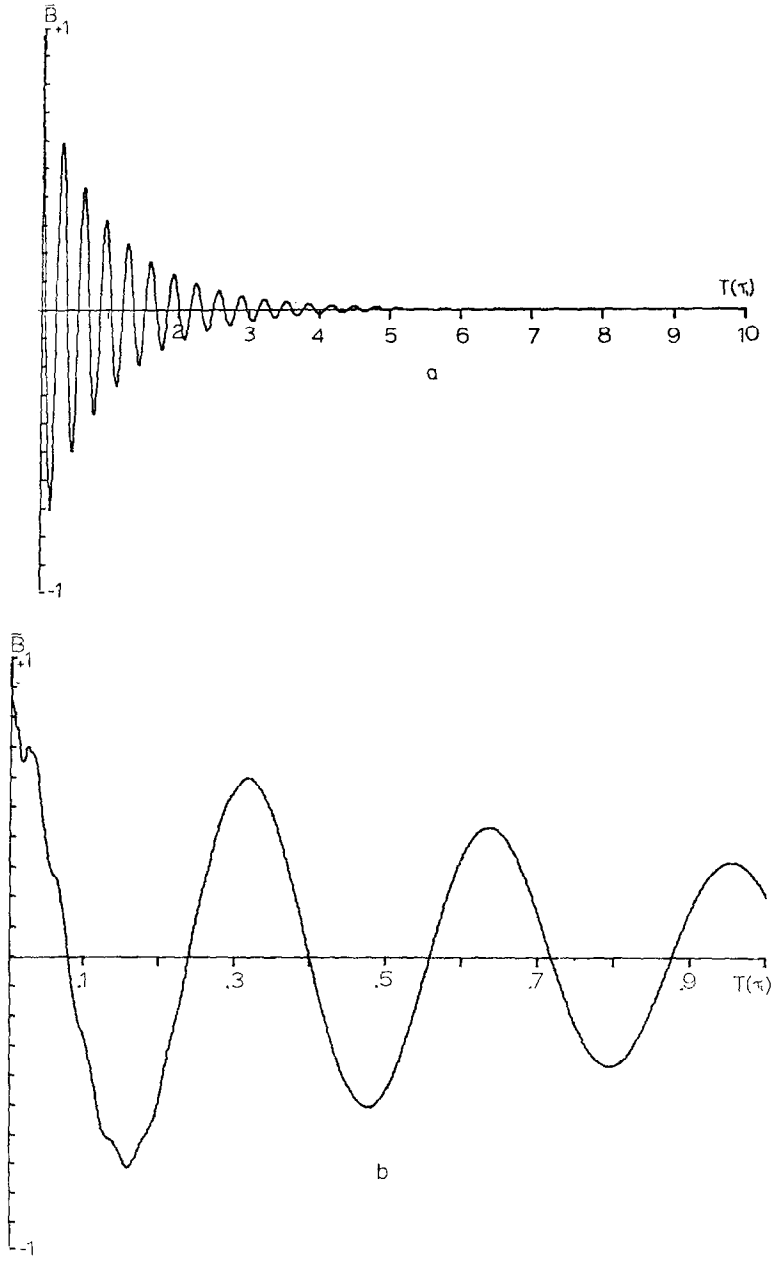

FIG. 4. The step-field response of an infinite plate (under the assumption of a free electron gas) using the analytic solutions.

For this infinite plate geometry we can simplify the program strategy. This simplification is allowed because we know that, in the absence of drive fields, the helicon fields go to zero at the boundary. The only solution of (5) which matches this boundary condition has the vacuum fields themselves zero for all time. Thus we can bypass Steps 2 and 3 of the strategy in accord with

$$B(z, t) = 0 \quad \text{for} \quad |z| \geqslant (c/2), t \geqslant 0. \tag{17}$$

Comparison of Results

The quantity μ calculated numerically by applying Eqs. (16a), (16b), and (16c) and its Fourier transform, the continuous wave response, are plotted in Figs. 2 and 3 respectively. The analytic solution (14) is plotted in Fig. 4 for comparison. Figure 5 is the Fourier transform of the curve of Fig. 4. Several actual field distributions at specific times are given in Fig. 6. Here the numeric solution and the analytic solution are superimposed.

These figures show that the numeric solution is a very good approximation to the analytic solution. The agreement becomes even better for smaller grid spacing and smaller time step.

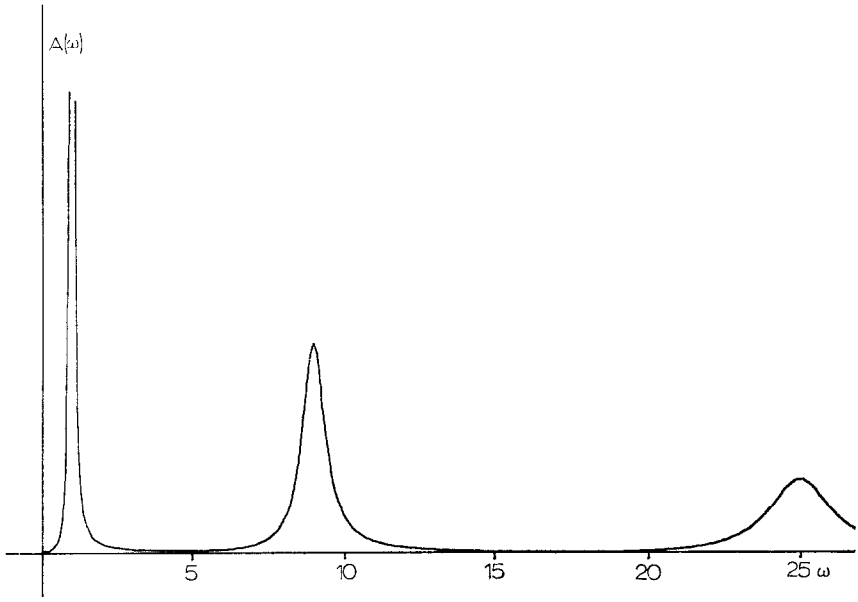

FIG. 5. The continuous wave response of an infinite plate (under the assumption of a free electron gas). The Fourier transform of the analytic solution.

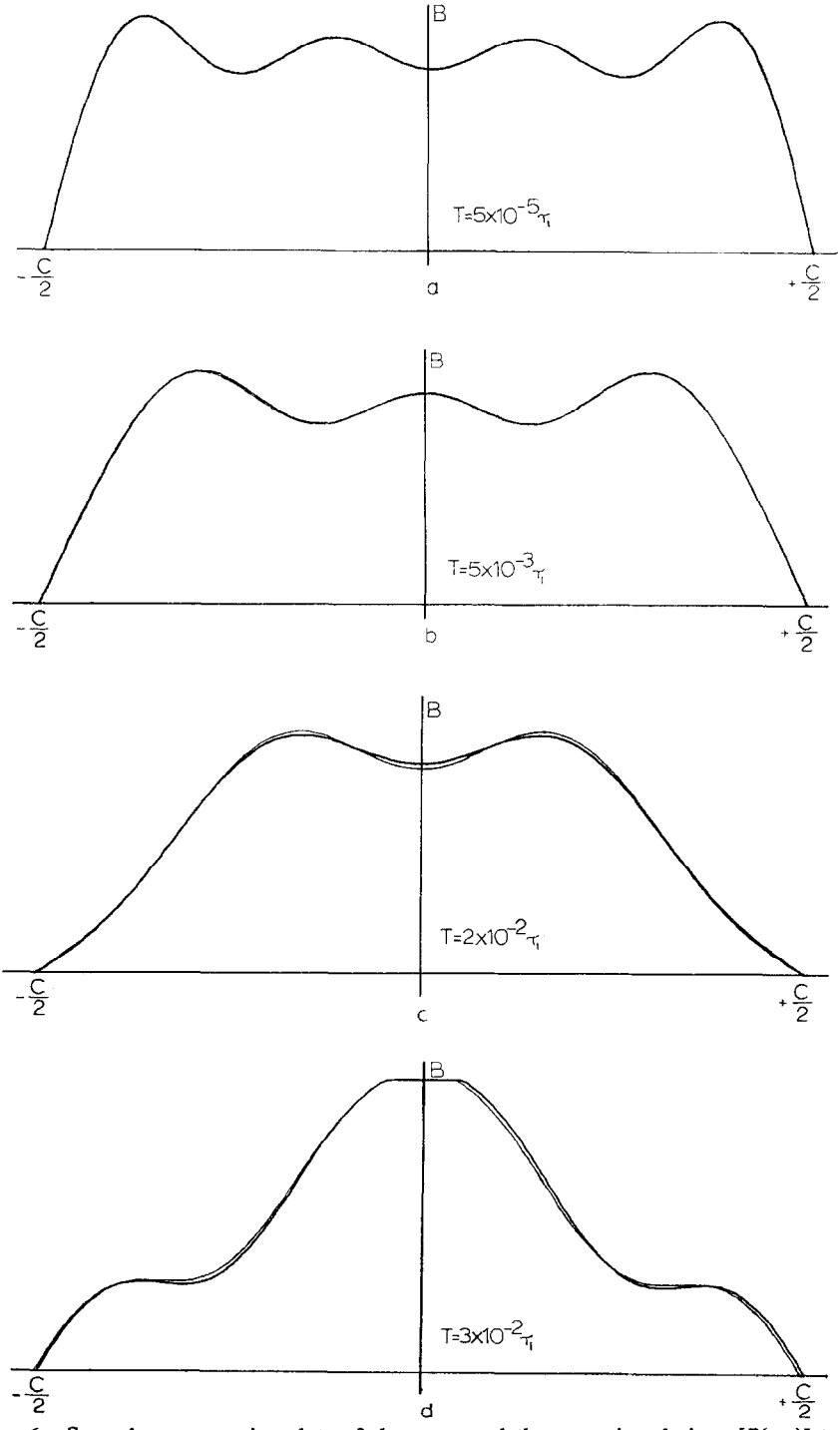

FIG. 6. Several representative plots of the exact and the numeric solutions $[B(z, t)]$ to the infinite plate helicon problems. The times are indicated on the plots. A free electron gas model is assumed.

4. Application to the Finite Plate

Formulation of Step 3 of the Strategy.

The formulation of the problem for finite geometries includes all the aspects of the infinite geometry already discussed. A number of other aspects must now be discussed. For the finite sample geometry no simplification of program strategy is allowed. Outside the sample, in free space, we must satisfy Eq. (5). This consists of the solution of three independent, potential-like problems in the variables B_x, B_y and B_z. The solution for one of the field quantities, say B_x, is found by making the Dufort and Frankel substitutions, Eq. (8), into the partial differential equation (5). Solving for unknown terms we find

$$B(N+1,1,I,J,K) = \Big(\frac{B(N,1,I+1,J,K)+B(N,1,I-1,J,K)}{\Delta X^2} + \frac{B(N,1,I,J,K+1)+B(N,1,I,J,K-1)}{\Delta Z^2} + \frac{B(N,1,I,J+1,K)+B(N,1,I,J-1,K)}{\Delta Y^2}\Big) \Big/ \Big(\frac{2}{\Delta X^2}+\frac{2}{\Delta Y^2}+\frac{2}{\Delta Z^2}\Big). \tag{18}$$

Here I, J, K correspond to the x, y, z position of the point referred to an origin at the geometric center of the sample. From symmetry we deal with only the first quadrant. Similarly the equations in B_y and B_z can be solved. The results are identical to those for B_x with the component subscripts changed to 2 and 3 respectively. It is only necessary to retain two time levels at once, levels N and $N+1$. This is an important consideration due to storage limitations.

Repeated application of (18) to all points outside the sample will yield a better approximation to the true solution. This is a relaxation method. Relaxation methods are routinely used to solve potential problems. This repeated iteration gives a better and better match to the boundary conditions. It has been found that after five applications of this scheme, the values near the surface show very little change (typically less than 1/2%). These boundary values are just the values needed by the helicon equation.

Formulation of Step 4 of the Strategy

The helicon equation is expanded in the Appendix. For the jellium model (free electron model) terms involving ρ_{13}, ρ_{23}, ρ_{31} and ρ_{32} will not appear.

The method of Dufort and Frankel is generalized by the addition of

$$\frac{d^2B_x}{dX\,dY} = \frac{\begin{pmatrix} B(N, 1, I+1, J+1, K) - B(N, 1, I+1, J-1, K) \\ - B(N, 1, I-1, J+1, K) + B(N, 1, I-1, J-1, K) \end{pmatrix}}{4\Delta X\,\Delta Y}. \quad (18a)$$

With these substitutions, Eqs. (18) and (18a), the helicon equation reduces to three coupled equations in the three unknowns $B(N+1, 1, I, J, K)$ and $B(N+1, 2, I, J, K)$ and $B(N+1, 3, I, J, K)$. These equations can be solved explicitly for the unknowns. Again the new time level $(N+1)$ can be stored over the old time level $(N-1)$.

Implementation

The rectangular sample had dimensions $c \times b \times b$. The ratio b/c is called the aspect ratio. The c dimension and the static field, B_0, are along the z axis. Point densities were selected to represent accurately the field configurations with $n = 1, 3$ and $1, m = 1, 3, 5$. The integers n, 1 and m are the numbers of half sine waves present along the z, x, and y axis, respectively. Although an initial field pattern including only these 1, m, n modes is not a uniform field across the sample, it is sufficiently complicated to demonstrate the field shapes in minor modes ($l, m > 1$) as well as major modes ($l = m = 1$).

Lattice points were chosen so that the point associated with the subscripts $I, J, K = 1, 1, 1$ was at the origin. The sample had 21, 21, and 11 points along the x, y and z axis, respectively. This means that points with subscripts $K \leqslant 6, J \leqslant 11$ or $I \leqslant 11$ are inside the sample. These 726 inside lattice points are sufficient to represent the $n = 1, 3$; $l, m = 1, 3, 5$ modes accurately. On the other hand, a total grid of 3000 lattice points is about as large as it can be and still iterate a fair number of times over the whole space.

TABLE I

Resources Required for the Finite Sample

	Lattice points	Storage	Time/iter	Time/step
Inside	726	4356	2.1 sec	2.1 sec
Outside	2742	16452	0.9 sec	4.5 sec
Program	—	7000	approx. 0	0.15 sec
Total	3468	17808	—	6.75 sec

Table I summarizes the resources required for the solution of the finite sample boundary value problem and the computer times necessary on a GEG35 system.

The elapsed time and field matrix were stored on magnetic tape between runs as indicated by Step 7 of the strategy. A run will automatically terminate when a chosen number of iterations have been completed. The program was structured in this way to make it fit scheduling restrictions. This structuring also allowed the results to be checked periodically. An average run was completed after about 1.5 hours of C.P.U. (Central Processor Unit) time. This scheme is implemented by program PROG7 and is available on request from the authors [6].

Results for the Finite Sample

Several runs on the finite sample are reported. The parameters of three typical runs are summarized in Table II.

TABLE II

Summary of the Parameters Used in Three Runs on the Finite Sample

	Run 1	Run 2	Run 3
ΔX	0.05	0.05	0.05
ΔY	0.05	0.05	0.05
ΔZ	0.1	0.1	0.1
ΔT	0.001	0.00025	0.004
u	20	100	20
λ	4	4	4
b/c	10	10	3
c	1	1	1

The permeabilities computed in each of these typical cases are displayed in Fig. 7. In all cases, the time axis is in the same units as were used for the infinite plate, τ_1. A number of runs have shown that there is no correlation between the step size in time, ΔT, and the actual flow of time, so the solution is not being driven by the iterative procedure. Runs with a number of different grid spacings have demonstrated that convergence is quite fast, but that, in order to represent accurately any given sine wave, a minimum of seven points across one half wavelength is useful. This criterion set the spatial grid step size.

The solution for the finite parallelepiped can be tested in a number of ways. First, the fit of the solution inside the sample to that outside can be checked at the surface. This fit is always better than 1 % and could be made arbitrarily small by multiple iterations over the exterior point grid. The external potential problem converged very satisfactorily.

Second, each principal mode of the step-field response should decay to $1/e$ of its initial value in $u/2\pi$ cycles (approximately). The argument for such a decay is based on the energy expended per cycle in each independent mode. The mode solutions

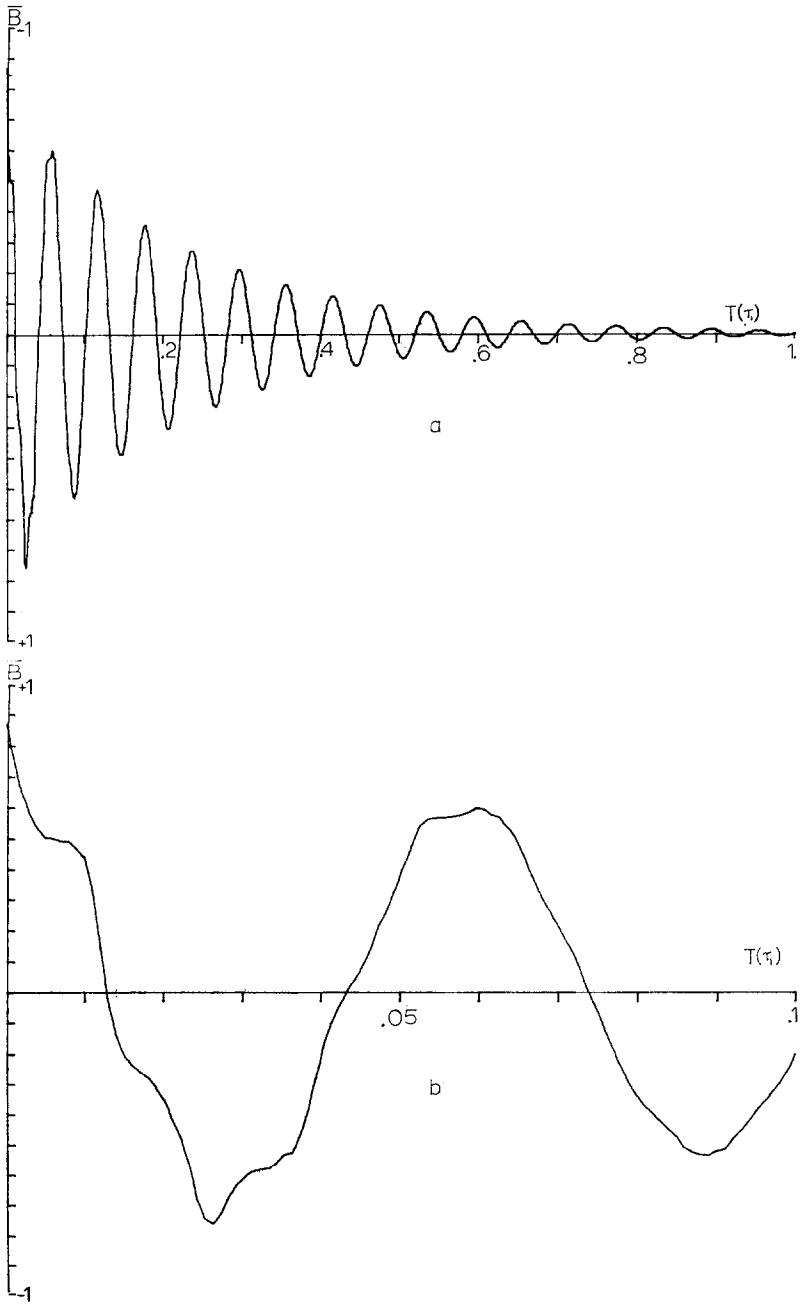

FIGURE 7

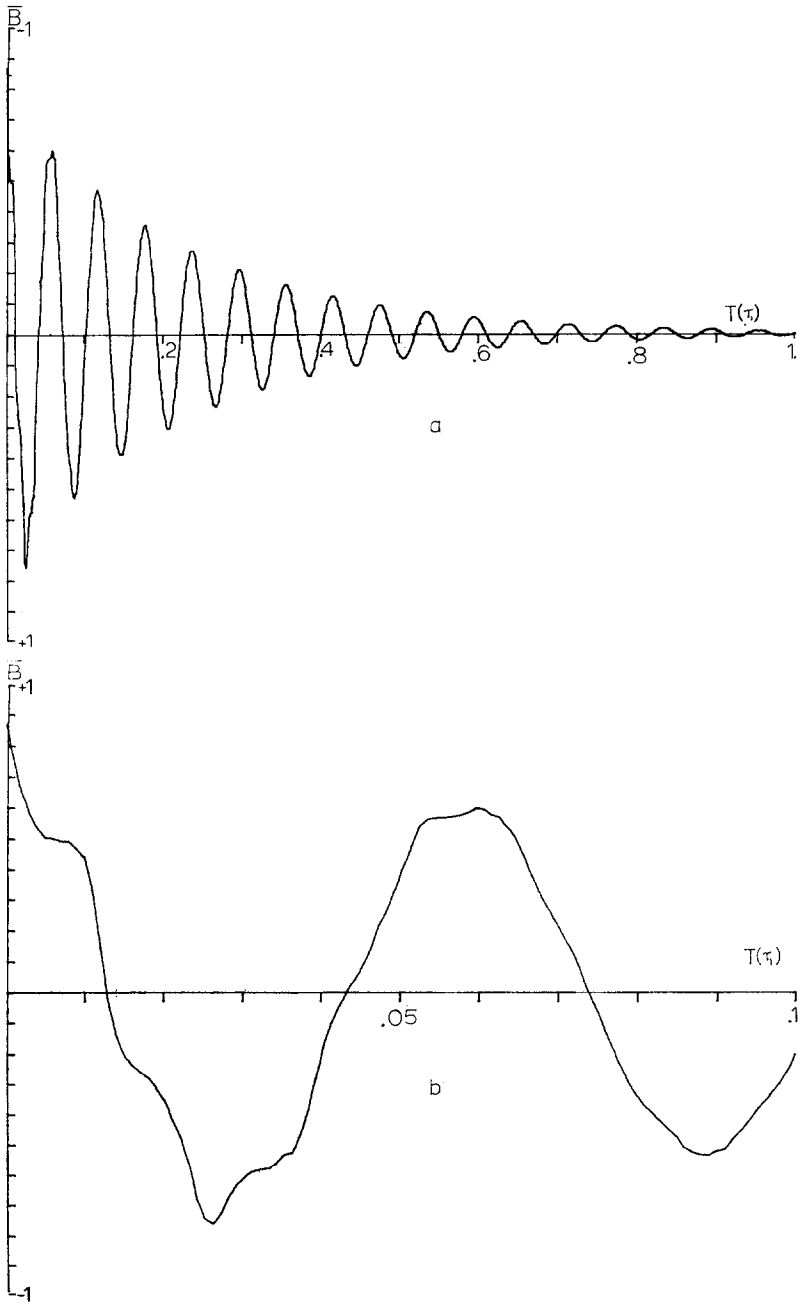

FIGURE 7

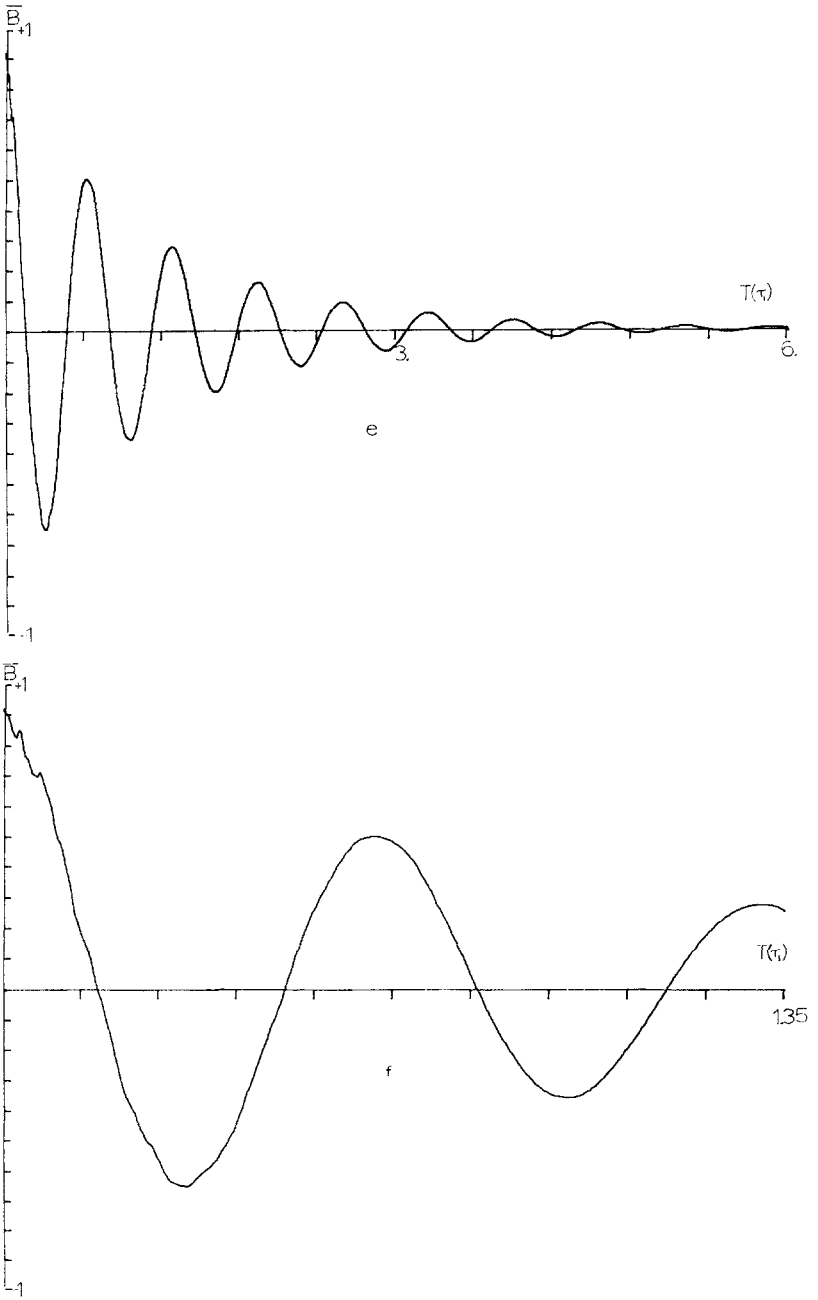

FIG. 7. The step-field response of 3 finite samples. The initial conditions for the curves are listed in Table II of the text. (a) and (b) are the response of a $10 \times 10 \times 1$ sample with $u = 20$. (c) and (d) are the same sample with $u = 100$. (e) and (f) are the response of a $4 \times 4 \times 1$ sample with $u = 20$.

do in fact decay in $u/2\pi$ cycles of oscillation. Since the time evolution of the field patterns obeys few general criteria, it is satisfying that the numerical solution agrees with those demands that exist.

One of the most interesting predictions from experiment [7] is that the field patterns inside the parallelepiped should exhibit mode structure in the directions perpendicular to the magnetic field. It was because of this experimental result that the rectangular parallelepiped geometry was the first studied by the numerical method. A mode having mode numbers $1 = m = 3$ and $n = 1$ should have (approximately) three half waves inside the sample in each of the directions transverse to B and one half wavelength along B. The solutions exhibit this behavior, but the amplitudes of these modes were quite small. A simple argument shows that the relative strengths of these modes should go as $1/l^2m^2$, and the numerical solution shows even smaller amplitudes especially near the sample edge. Nonetheless these minor modes are present in the solution.

The most sensitive test of the existence of these minor modes would be to run the time response out far enough to see the beating of the 1, 3, 1 mode with the 1, 1, 1 mode (as observed experimentally in Ref. [7]). To run the numerical solution that long (many times the reciprocal of the difference in frequencies for the modes) is prohibitively expensive.

Figure 7a shows the response of a $10 \times 10 \times 1$ parallelepiped with a u of 20. Such a sample might be a $10 \times 10 \times 1$ mm Na slab with an 8000 resistivity ratio in a magnetic field of about 10 kG. Such samples have been used in the experimental study of the helicon boundary value problem. Figure 7a shows the oscillatory response of the permeability μ in the x direction over many cycles so that the decay of the circularly polarized wave is clear. The decay rate is correct for a u of 20. Figure 7b shows the first portion of the oscillations in Fig. 7a on a shorter time scale. The oscillations from the $n = 3$ mode, with approximately three half waves fitting parallel to B in the sample, appear as small bumps on $n = 1$ oscillations (cf. Fig. 4 in Ref. [7]).

Figure 7c examines the same sample in a higher magnetic field. The parameter u is now 100, and the time step ΔT must be correspondingly smaller in order to follow the oscillations. The decay rate is that predicted by the energy argument. Figure 7d is a closer look at the first few oscillations of Fig. 7c. The complicated bumps superimposed on the $n = 1$ oscillations are the $n = 3$ and the $n = 5$ modes. These modes decay in the same number of cycles as does the $n = 1$.

Figures 7e and 7f show the same sorts of results for a sample of smaller aspect ratio. This sample is $4 \times 4 \times 1$ and is the sample in which minor mode structure is most apparent. Again the decays of the $n = 1$ and $n = 3$ modes are correct. The minor modes are too small to be seen in these permeabilities. The calculation of permeabilities averages the field over the sample and tends to obscure small oscillations in the internal wave fields.

5. Conclusion

The methods of finite differences have been applied to the solution of the helicon equation for two geometries. In the case of an infinite plate, excellent agreement with the analytic solution of Chambers and Jones was found. There are no analytic solutions to finite geometry problems so most of the physical checks upon the numerical method must be made for the infinite plate. The numerical solution passes all these checks.

One geometry with finite dimensions was considered. This geometry was the finite rectangular parallelepiped. Most of the experiments using the helicon to investigate the topology of Fermi Surfaces have used such parallelepipeds. This present work demonstrates that the boundary value problem for the helicon is well enough understood to continue these experiments. Qualitative and semiquantitative agreement was found. The numerical method is an extension of that applied to the infinite geometry. The approach described is capable of accepting both an arbitrary resistivity tensor and an arbitrary geometry. The fact that a boundary value problem as complicated as the helicon problem can be handled by a finite difference technique without demonstrating instabilities is important. Given enough computer time, this method of solution can produce the response of any sample to arbitrary accuracy. For these reasons the method of finite differences may be valuable as an independent check against experiment and as a test of many particular models of Fermi surface shape in pure metals.

Appendix: Expansion of the Helicon Equation $\nabla \times (\rho \nabla \times \mathbf{B}) = -\mu_0(\partial \mathbf{B}/\partial t)$ in Rectangular Coordinates

$$\nabla \times (\rho \nabla \times \mathbf{B}) = -\mu_0 \frac{\partial \mathbf{B}}{\partial t},$$

where

$$\rho = \begin{pmatrix} \rho_{11} & \rho_{12} & \rho_{13} \\ \rho_{21} & \rho_{22} & \rho_{23} \\ \rho_{31} & \rho_{32} & \rho_{33} \end{pmatrix},$$

$$\mathbf{B} = B_x\hat{x} + B_y\hat{y} + B_z\hat{z}.$$

l.h.s.

$$\nabla \times \mathbf{B} = \begin{pmatrix} \hat{x} & \hat{y} & \hat{z} \\ \frac{\partial}{\partial x} & \frac{\partial}{\partial y} & \frac{\partial}{\partial z} \\ B_x & B_y & B_z \end{pmatrix}$$

$$= \hat{x}\left(\frac{\partial B_z}{\partial y} - \frac{\partial B_y}{\partial z}\right) + \hat{y}\left(\frac{\partial B_x}{\partial z} - \frac{\partial B_z}{\partial x}\right) + \hat{z}\left(\frac{\partial B_y}{\partial x} - \frac{\partial B_x}{\partial y}\right).$$

$$\rho(\nabla \times \mathbf{B}) = \begin{pmatrix} \rho_{11} & \rho_{12} & \rho_{13} \\ \rho_{21} & \rho_{22} & \rho_{23} \\ \rho_{31} & \rho_{32} & \rho_{33} \end{pmatrix} \begin{pmatrix} \dfrac{\partial B_z}{\partial y} - \dfrac{\partial B_y}{\partial z} \\ \dfrac{\partial B_x}{\partial z} - \dfrac{\partial B_z}{\partial x} \\ \dfrac{\partial B_y}{\partial x} - \dfrac{\partial B_x}{\partial y} \end{pmatrix}$$

$$= \hat{x}\left[\rho_{11}\left(\frac{\partial B_z}{\partial y} - \frac{\partial B_y}{\partial z}\right) + \rho_{12}\left(\frac{\partial B_x}{\partial z} - \frac{\partial B_z}{\partial x}\right) + \rho_{13}\left(\frac{\partial B_y}{\partial x} - \frac{\partial B_x}{\partial y}\right)\right]$$

$$+ \hat{y}\left[\rho_{21}\left(\frac{\partial B_z}{\partial y} - \frac{\partial B_y}{\partial z}\right) + \rho_{22}\left(\frac{\partial B_x}{\partial z} - \frac{\partial B_z}{\partial x}\right) + \rho_{23}\left(\frac{\partial B_y}{\partial x} - \frac{\partial B_x}{\partial y}\right)\right]$$

$$+ \hat{z}\left[\rho_{31}\left(\frac{\partial B_z}{\partial y} - \frac{\partial B_y}{\partial z}\right) + \rho_{32}\left(\frac{\partial B_x}{\partial z} - \frac{\partial B_z}{\partial x}\right) + \rho_{33}\left(\frac{\partial B_y}{\partial x} - \frac{\partial B_x}{\partial u}\right)\right].$$

$\nabla \times (\rho \nabla \times \mathbf{B})$

$$= \hat{x}\left[\rho_{31}\left(\frac{\partial^2 B_z}{\partial y^2} - \frac{\partial^2 B_y}{\partial y\,\partial z}\right) + \rho_{32}\left(\frac{\partial^2 B_x}{\partial y\,\partial z} - \frac{\partial^2 B_z}{\partial y\,\partial x}\right) + \rho_{33}\left(\frac{\partial^2 B_y}{\partial x\,\partial y} - \frac{\partial^2 B_x}{\partial y^2}\right)\right.$$

$$\left. - \rho_{21}\left(\frac{\partial^2 B_z}{\partial y\,\partial z} - \frac{\partial^2 B_y}{\partial z^2}\right) - \rho_{22}\left(\frac{\partial^2 B_x}{\partial z^2} - \frac{\partial^2 B_z}{\partial x\,\partial z}\right) - \rho_{23}\left(\frac{\partial^2 B_y}{\partial x\,\partial z} - \frac{\partial^2 B_x}{\partial z\,\partial y}\right)\right]$$

$$+ \hat{y}\left[\rho_{11}\left(\frac{\partial^2 B_z}{\partial y\,\partial z} - \frac{\partial^2 B_y}{\partial z^2}\right) + \rho_{12}\left(\frac{\partial^2 B_x}{\partial z^2} - \frac{\partial^2 B_z}{\partial x\,\partial z}\right) + \rho_{13}\left(\frac{\partial^2 B_y}{\partial x\,\partial z} - \frac{\partial^2 B_x}{\partial y\,\partial z}\right)\right.$$

$$\left. - \rho_{31}\left(\frac{\partial^2 B_z}{\partial x\,\partial y} - \frac{\partial^2 B_y}{\partial z\,\partial x}\right) - \rho_{32}\left(\frac{\partial^2 B_x}{\partial z\,\partial x} - \frac{\partial^2 B_z}{\partial x^2}\right) - \rho_{33}\left(\frac{\partial^2 B_y}{\partial x^2} - \frac{\partial^2 B_x}{\partial y\,\partial x}\right)\right]$$

$$+ \hat{z}\left[\rho_{21}\left(\frac{\partial^2 B_z}{\partial y\,\partial x} - \frac{\partial^2 B_y}{\partial z\,\partial x}\right) + \rho_{22}\left(\frac{\partial^2 B_x}{\partial z\,\partial x} - \frac{\partial^2 B_z}{\partial x\,\partial y}\right) + \rho_{33}\left(\frac{\partial^2 B_y}{\partial x^2} - \frac{\partial^2 B_x}{\partial y\,\partial x}\right)\right.$$

$$\left. - \rho_{11}\left(\frac{\partial^2 B_z}{\partial y^2} - \frac{\partial^2 B_y}{\partial z\,\partial y}\right) - \rho_{12}\left(\frac{\partial^2 B_x}{\partial z\,\partial y} - \frac{\partial^2 B_z}{\partial x\,\partial y}\right) - \rho_{13}\left(\frac{\partial^2 B_y}{\partial x\,\partial y} - \frac{\partial^2 B_x}{\partial y^2}\right)\right].$$

r.h.s.

$$-\mu_0 \frac{\partial \mathbf{B}}{\partial t} = -\mu_0 \frac{\partial B_x}{\partial t}\hat{x} - \mu_0 \frac{\partial B_y}{\partial t}\hat{y} - \mu_0 \frac{\partial B_z}{\partial t}\hat{z}.$$

Equating r.h.s. and l.h.s. yields three equations in three unknowns (B_x, B_y, B_z)

REFERENCES

1. C. R. LEGENDY, *J. Math. Phys.* **6** (1965), 153.
2. C. R. LEGENDY, *Phys. Rev.* **135** (6A) (1964), 1717.
3. R. G. CHAMBERS AND B. K. JONES, *Proc. Roy. Soc. (London)* **A270** (1962), 417.
4. P. D. LAX AND R. D. RICHTMEYER, *Commun. Pure Appl. Math.* **9** (1956), 267.
5. E. C. DUFORT AND S. P. FRANKEL, *Math. tables and other aids to computation* **7** (1953), 139.
6. N. L. WENTLAND, "Numeric Solution of the Helicon Boundary Value Problem," Master's thesis, Dartmouth College, Hanover, NH, 1970.
7. J. R. MERRILL, M. T. TAYLOR AND J. M. GOODMAN, *Phys. Rev.* **131** (1963), 2499.